Chemical Science

ROYAL SOCIETY OF CHEMISTRY

EDGE ARTICLE

View Article Online
View Journal | View Issue

Cite this: *Chem. Sci.*, 2022, **13**, 11110

All publication charges for this article have been paid for by the Royal Society of Chemistry

Received 28th July 2022
Accepted 26th August 2022

DOI: 10.1039/d2sc04204e

rsc.li/chemical-science

Snapshots of key intermediates unveiling the growth from silver ions to Ag_{70} nanoclusters†

Xi-Ming Luo, [a] Shuo Huang,[a] Peng Luo,[b] Kai Ma,[a] Zhao-Yang Wang,[a] Xi-Yan Dong [ab] and Shuang-Quan Zang *[a]

Nanoclusters (NCs) are considered as initial states of condensed matter, and unveiling their formation mechanism is of great importance for directional synthesis of nanomaterials. Here, we initiate the reaction of Ag(I) ions under weak reducing conditions. The prolonged reaction period provides a unique opportunity for revealing the five stages of the growth mechanism of 20-electron superatomic **Ag_{70}** NCs by a time-dependent mass technique, that is, aggregate (I) → reduction (II) → decomposition and recombination (III) → fusion (IV) → surface recombination and motif enrichment (V), which is different from the formation process applicable to the gold clusters. More importantly, the key intermediates, **Ag_{14}** without free electrons (0e) in the first (stage I) and **Ag_{24}** (4e) in the second (stage II), were crystallized and structurally resolved, and the later transformation rate towards **Ag_{70}** was further controlled by modulating solvents for easy identification of more intermediates. In a word, we establish a reasonable path of gradual expansion in size and electrons from Ag(I) ions to medium-sized 20e **Ag_{70}**. This work provides new insights into the formation and evolution of silver NCs, and unveils the corresponding optical properties along with the process.

Introduction

Atomically precise coinage metal (M = Au,[1] Ag,[2] Cu[3]) nanoclusters as the bridges between atoms and nanoparticles,[4] which provide a unique opportunity for gaining fundamental knowledge of nanoparticles, are a newly emerging hot topic in nanoscience. Their diverse aesthetic structures with discrete energy levels and extensive modification greatly promote their increasing attraction in the fields of chirality,[5] luminescence,[6] catalysis,[7] sensing,[8] and biomedicine.[9] Clear identification of the grand evolution of structures and properties from discrete atoms to the metallic state, and the effectively controlled synthesis of intermediates of large-sized metal NCs remain tough tasks.[10] Xie and co-workers investigated the formation mechanism and evolution process of atomically precise thiolate-stabilized Au and Ag NCs from simple metal-thiolate precursors by real-time electrospray ionization-mass spectrometry (ESI-MS).[11] For gold NCs, the step-by-step formation process from Au(I)–SR monomers to oligomers to NCs has been revealed by using well-known model Au_{25}.[11e,f] Wang developed a facile approach to assemble different thiolate-stabilized Au_{25} with eight valence electrons (8e) in high yield (~100%) on a large scale, starting from a preformed Au_{13} (8e) crystalline material, showing that the formation of metal NCs can be achieved by forming stable metal cores and then enriching Au(I)–SR staples on the surface.[12] Generally, the most commonly used method for the preparation of "medium/large-sized" metal NCs (nucleus number more than 50) is the reduction of metal precursors with appropriate reducing agents (such as $NaBH_4$, Ph_2SiH_2, and the borane tertbutylamine complex).[13] The reduction process (M(I) → M(0)) is basically completed within a few minutes and this quick reduction process makes it difficult to capture the intermediates in the single crystal form.[11d–g]

The structure and size of silver NCs are considered to be mainly related to the number of silver atoms in the intermediate products.[11g] So far, the detailed process from silver ions to NCs, including the reduction and nucleation process for metal NCs is still a black box. Recently, we reported a 20e **Ag_{70}** nanocluster, ($[NH_2(CH_3)_2][Ag_{70}S_4(S^iPr)_{24}(CF_3COO)_{20}]$),[14] using DMF as a reductant. The slow reduction process to **Ag_{70}** in ten hours (Fig. 1) provides a platform to follow the growth process, capture intermediates and reveal the formation mechanism of the "medium-sized" silver NCs.

In this work, we carefully studied the formation of **Ag_{70}** (ref. 14) by time-dependent UV-vis spectroscopy and ESI-MS. By controlling the synthesis conditions, we successfully

[a]*Henan Key Laboratory of Crystalline Molecular Functional Materials, Henan International Joint Laboratory of Tumor Theranostical Cluster Materials, Green Catalysis Center, College of Chemistry, Zhengzhou University, Zhengzhou 450001, People's Republic of China. E-mail: zangsqzg@zzu.edu.cn*

[b]*College of Chemistry and Chemical Engineering, Henan Polytechnic University, Jiaozuo 454003, People's Republic of China*

† Electronic supplementary information (ESI) available: Fig. S1–S31 and Tables S1–S9 for experimental details, detailed crystallographic structures, DFT, UV, ESI-MS, and crystal data of nanoclusters. CCDC 2182448, 2182449, and 2182450. For ESI and crystallographic data in CIF or other electronic format see https://doi.org/10.1039/d2sc04204e

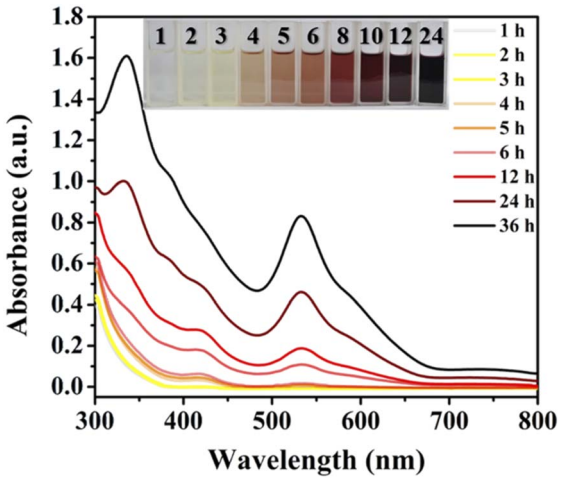

Fig. 1 Time-dependent UV-vis absorption spectra for tracking the reaction process. Experimental method: 9 mg $\{Ag(S^iPr)\}_n$, 22 mg CF_3COOAg, and 50 μL CF_3COOH in the solvent mixture (^{i}PrOH : DMF = 3 : 1) at 80 °C. Inset: the colour of mother liquor after the solvothermal reaction at different times (1–24 h).

crystallized the key species $Ag_{24}S(S^iPr)_8(CF_3COO)_{10}(DMF)_{10}$ (denoted as **Ag_{24}**) with four valence electrons (4e). **Ag_{24}** has two relatively independent delocalized centers Ag_6^{4+}, separated by an anion-template S^{2-}. Time-dependent ESI-MS and the mass difference fingerprint of isomorphism (MDFI) method unveil the transformation process from Ag(I) ions, 4e **Ag_{24}** to 20e **Ag_{70}**. Careful analysis based on the experimental data shows that **Ag_{70}** is not directly formed *via* DMF reduction from Ag(I) ions or pre-generated Ag(I)–S aggregates with a similar size, but generated through a cascade of reactions of the intermediates, including aggregation, reduction, decomposition, recombination, fusion, surface recombination and motif enrichment. The formation mechanism of the medium-sized silver NCs is instructive and meaningful in revealing the essence of the original state of metal nanoparticles.

Results and discussion

Tracking the growth process of Ag_{70}

Identification of the intermediate species by the high-resolution ESI-MS technique during the reduction process is a straightforward and effective method to elucidate the growth mechanism of metallic NCs, which has been achieved in the synthesis of classic gold clusters.[11a–f,12] However, the complexity of the reaction system and the mutable inherence of silver intermediate species hinder the in-depth study of Ag NCs. Little progress based on the structural evolution and size expansion of Ag^0-containing homosilver NCs is reported.[11g] Recently, it was found that the reaction solution of the superatomic Ag NC (**Ag_{70}**) reported by our group has obvious color changes (from yellow to red (black), Fig. 1) at different times, and there may be intermediate products which are beneficial to explore the growth process of **Ag_{70}**.

A series of improved experiments were carried out to achieve our goal (Fig. S1–S5, see details in the ESI†). Using different reaction times or conditions to control the reduction process, the color of the mother liquor is significantly different (Fig. 1), which indicates that the reduction degree of the system gradually deepened. The thiol (HSR) and carboxylic acid (R′COOH) ligands used in the system were finely adjusted (R: $-CH(CH_3)_2 \rightarrow -CH(CH_3)(CH_2CH_3)$; R′: $-CF_3 \rightarrow -CF_2CF_3$) and a similar phenomenon emerged in an attempt to characterize the generality of the process and identify some intermediates by the MDFI method (Fig. S6†). The solution components of the above-mentioned reaction were monitored by ESI-MS.

Determination of intermediates by the mass difference fingerprint of isomorphism (MDFI) method

Identifying meaningful unknown species with large masses (m/z > 2000) based on the ESI-MS data is a great challenge. By unrestrictedly matching m/z values, a lot of irreducible results can be obtained within the range of the allowable error. Of course, common methods (isotope (H/D) labeling) of determining H^- in H-rich metal NCs can be used, but at an unquestionably high cost. Inspired by a study on the hydrolysis process of lanthanide (Ln^{3+}) clusters, to accurately determine the amount of a component of the species corresponding to the peaks from the ESI-MS data, an MDFI method that utilizes a certain mass difference of similar ligands to determine the exact number of the corresponding components in different species is proposed.[15] This method is based on the fact that similar experimental phenomena can still be observed when the relevant ligands (R: $-CH(CH_3)_2 \rightarrow -CH(CH_3)(CH_2CH_3)$ or R′: $-CF_3 \rightarrow -CF_2CF_3$) are changed in the reaction system (Fig. S6†). This result has inspired an encouraging speculation that they may have the same/similar growth process from an Ag^+ ion to the target NC and intermediates during their formation. This MDFI method plays an important role in the subsequent identification of key intermediates (Scheme 1). For example, as

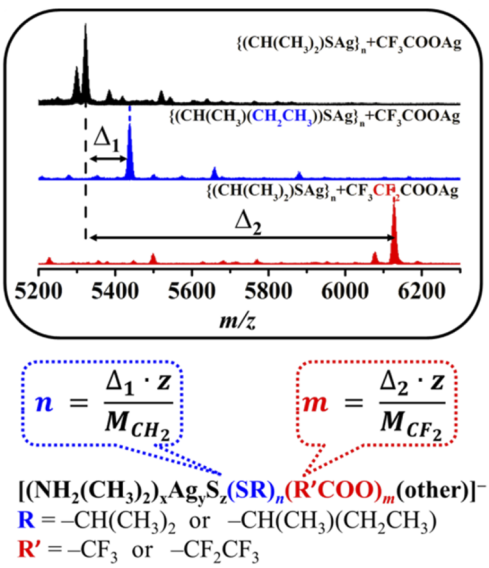

Scheme 1 Determination of key intermediates by the mass difference fingerprint of isomorphism (MDFI) method. z is the charge.

shown in Scheme 1, a peak observed in the ESI-MS spectrum of the $\{^{i}PrSAg\}_n$ + CF_3COOAg system includes n $^{i}PrS^-$ and m CF_3COO^- ligands, and the analogue including n $CH(CH_3)(CH_2CH_3)S^-$ or m $C_2F_5COO^-$ may be observed in the ESI-MS spectrum for $\{CH(CH_3)(CH_2CH_3)SAg\}_n$ + CF_3COOAg or $\{^{i}PrSAg\}_n$ + C_2F_5COOAg systems (Fig. 3 and S7, S8†), where only one variable was changed (Scheme 1). Thus, based on the mass difference (Δ_1 and Δ_2) and charges (z), the number (n and m) of related ligands ($^{i}PrS^-$ and CF_3COO^-) can be easily determined by using the related equation in Scheme 1. Note that this MDFI method is only used to rule out irreducible results. However, due to the presence of different ligands, it is normal that the peaks of related clusters do not conform to this phenomenon. For example, no peaks corresponding to the final product ($[Ag_{70}S_4(SCH(CH_3)(CH_2CH_3))_{24}(CF_3COO)_{20}]^{2-}$) were found (Fig. S6a†).

Species assignment in solution

The time-dependent UV-vis spectra (Fig. 1) showed that the characteristic peak (*ca.* 530 nm) of **Ag_{70}** appeared after 4 h (Fig. S1†), corresponding to the color change of the mother liquor from yellow to orange. Interestingly, when the mother liquor changed to yellow (reaction time: 2–3 h), only a sharp characteristic absorption peak (416 nm) did not belong to **Ag_{70}** (Fig. S1d†), suggesting that intermediate substances may have been formed during the formation of **Ag_{70}**.

Time-dependent ESI-MS (Fig. 2 and S7, S8†) is used to confirm the presence of possible intermediates. Due to the complexity of the spectra and the presence of a large number of peaks, we focused on those peaks that appeared and intensified as the reaction proceeded. According to the real-time ESI-MS spectra, small Ag^{I}_n clusters protected by organic ligands ($S^{i}Pr^-$ and CF_3COO^-), such as $[NH_2(CH_3)_2]_x[Ag_{12+y}(S^{i}Pr)_6(CF_3COO)_{7+x+y}]^-$ (x = 0–4, y = 0–3), existed in the reaction solution from the beginning to the end (Fig. S7–S9†). After 12 h, clear peaks corresponding to **Ag_{70}** (Fig. S7†) began to appear at m/z = 5800–6300 assignable to $[NH_2(CH_3)_2]_x[Ag_{70}S_4(S^{i}Pr)_{24}(CF_3COO)_{20+x}]^{2-}$ (x = 0–4), which was consistent with the UV-vis results. Furthermore, the partial remaining peaks differ by a fixed value, 220 (assigned to CF_3COOAg) and 159 (assigned to $[NH_2(CH_3)_2CF_3COO]$), which also fully indicates that these small molecules are easily enriched on the surface of clusters in the mother liquor. An obvious peak of m/z = 5322.82 attracted our attention, and its intensity gradually increased with the reaction time (2–12 h, Fig. 2b). Then it gradually decreased with the increase of **Ag_{70}** until it disappeared. This species is likely to be the intermediate/transition state that we are looking for. By employing the MDFI method, the number of SR^- and $R'COO^-$ in this peak could be easily determined, and finally assigned to $[NH_2(CH_3)_2]_4[Ag_{25}S(SR)_8(R'COO)_{16}]^-$ (denoted as $\{Ag_{25}S\}$, R = $-CH(CH_3)_2$ or $-CH(CH_3)(CH_2CH_3)$; R′ = $-CF_3$ or $-CF_2CF_3$; Fig. S6†). From the composition of the $\{Ag_{25}S\}$ cluster, it was found that it has four free valence electrons and one S^{2-}, which may be the product of the reduction of monovalent Ag–S aggregates.

In addition to this $\{Ag_{25}S\}$ (4e) species, another group of species with 9 free electrons, $\{[NH_2(CH_3)_2]_3[Ag_{21+x}(S^{i}Pr)_5(CF_3COO)_{11+x}]\}^-$ (x = 0–2, denoted as $\{Ag_{21}\}$, $\{Ag_{22}\}$, and $\{Ag_{23}\}$), was observed. As observed in the intensity curve based on the ESI-MS data in Fig. 2b, $\{Ag_{25}S\}$ species was the dominant product. It appeared after three hours of reaction and continued to increase as the reaction proceeded until it began to decrease after 18 hours. The $\{Ag_{23}\}$ species exhibited a similar trend in the concentration curve, which means that it may have been transformed from $\{Ag_{25}S\}$ species, and the increase in the number of free electrons is also reasonable. The intensities of $\{Ag_{21}\}$, $\{Ag_{22}\}$, and $\{Ag_{70}S_4\}$ species have increased since their appearance, and especially the curves of $\{Ag_{21}\}$, and $\{Ag_{70}S_4\}$ have the same trend (Fig. 2b). A similar phenomenon (Fig. S8†) was also observed during the reaction of increasing $\{Ag(S^{i}Pr)\}_n$. So, the evolution of $\{Ag_{70}S_4\}$ may follow such a path: $\{Ag_{12-15}\}$ (0e) → $\{Ag_{25}S\}$ (4e) → $\{Ag_{21-23}\}$ (9e) → $\{Ag_{70}S_4\}$ (20e), and the related detailed discussion is in the following part. Unfortunately, there is not much information available in positive ion mode ESI-MS to deepen our understanding of this process.

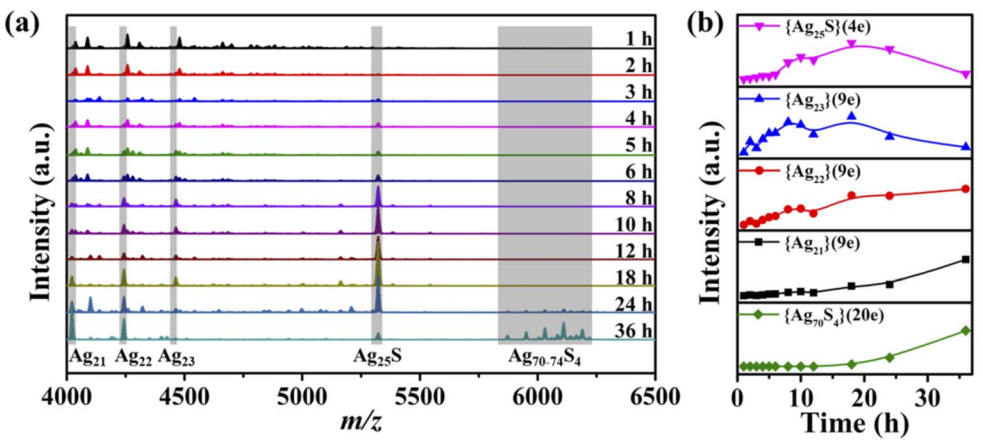

Fig. 2 Time-dependent ESI-MS spectra for the reaction solutions. (a) Negative ion mode ESI-MS data in the m/z range of 4000–6500 for the reaction solutions of 9 mg $\{Ag(S^{i}Pr)\}_n$, 22 mg CF_3COOAg, and 50 μL CF_3COOH in the solvent mixture ($^{i}PrOH$: DMF = 3 : 1) at 80 °C. (b) Intensity-based curves of $\{Ag_{25}S\}$, $\{Ag_{23}\}$, $\{Ag_{22}\}$, $\{Ag_{21}\}$, and $\{Ag_{70}S_4\}$. $\{Ag_{70}S_4\}$ = $[Ag_{70}S_4(S^{i}Pr)_{24}(CF_3COO)_{20}]^{2-}$.

Structural characterization

Based on ESI-MS analysis, considering the abundance increase of {$Ag_{25}S$} and other species in the early stage of the reaction, crystallization is quite helpful to determine their structures. Four kinds of crystals were obtained by evaporating the mother liquor at different reaction times at room temperature (Fig. S10†): colorless block (**Ag_{14}**, 0 h), yellow block (**Ag_{24}**, 3–6 h), black octahedral (**$Ag_{70}\cdot Ag_{12}$**, 8–24 h), and black rectangular (**Ag_{70}**, 36 h) crystals. If CF_3COOAg and CF_3COOH in the reaction are replaced by C_2F_5COOAg and C_2F_5COOH, respectively, two types of crystals were obtained: yellow block (**Ag_{24}-C_2F_5**, 3 h), and black rectangular (**Ag_{70}-C_2F_5**, 24 h) crystals.

The structures of the two black crystals (**$Ag_{70}\cdot Ag_{12}$** and **Ag_{70}**) have been analyzed in a previous work, and **Ag_{70}-C_2F_5** has the same structure (except for the different $R'COO^-$ ligands) and similar cell parameters as **Ag_{70}**; for more details please see ref. 14. The molecular structures of colorless (**Ag_{14}**, formula $Ag_{14}(S^iPr)_6(CF_3COO)_8(DMF)_6$) and yellow block crystals (**Ag_{24}**/**Ag_{24}-C_2F_5**, formula $Ag_{24}S(S^iPr)_8(R'COO)_{10}(DMF)_8 \cdot 2(NH_2(CH_3)_2R'COO)$, $R' = -CF_3$ or $-C_2F_5$) were determined by single-crystal X-ray diffraction (SCXRD) analysis (Tables S1–S3†) and elemental analysis. The structure of the {$Ag_{25}S$} species observed in ESI-MS should be **Ag_{24}** without DMF molecules, whose exposed parts are covered by additional CF_3COO^- and CF_3COOAg.

Ag_{14} features an ellipsoidal Ag(I) cluster (Fig. S11†). Except that the middle silver ring expands from six to eight Ag atoms, the silver–sulfur framework of **Ag_{14}** is similar to that of Ag_{12} in **$Ag_{70}\cdot Ag_{12}$** (Fig. S11†).[14]

Considering the structural similarity between **Ag_{24}** and **Ag_{24}-C_2F_5** (Fig. S12†), **Ag_{24}** was selected as the representative for illustration (Fig. 3). **Ag_{24}** crystallizes in a triclinic space group ($P\bar{1}$) and possesses half a cluster in the asymmetric unit (Fig. S12†). As is shown in Fig. 3a, the total structure of **Ag_{24}** presents a long strip shape, composed of one sulfur atom, 24 silver atoms, and organic ligands (eight S^iPr^-, ten CF_3COO^- and ten DMF molecules). The size of the "shuttle"-like $S@Ag_{24}$ framework (Fig. 3b) is $4.6 \times 4.6 \times 12.9$ Å^3. The μ_4-S^{2-} located in the inversion center (Fig. S13†) originates from the breaking of the S–C bond of S^iPr^-, and serves as an anion template here. The S^{2-}-template gathers 14 silver atoms together to form a slightly twisted cube (μ_4-$S@Ag_{14}$, Fig. 3d and S14a†), where Ag atoms occupy the vertices and the center of the faces (Ag–S bond lengths: 2.537(2) and 2.621(4) Å; the distances of Ag···Ag: 3.212(4) to 3.464(4) Å, Table S3†). Interestingly, two classical Ag_6 octahedra appear on both sides of the above polyhedron (Fig. 3c and S14b†). The three parts merge into the final skeleton ($Ag(S@Ag_{14})\cdots Ag(Ag_6)$: 3.057(3) to 3.171(3) Å) by sharing silver atoms (Fig. 3b). The 8 S^iPr^- ligands with a μ_4 mode, located at the junction of the $S@Ag_{14}$ fragment and the Ag_6 motifs, hold them firmly together (Fig. S13†). The Ag–S(S^iPr^-) bond lengths are located in the range of 2.395(6) to 2.576(9) Å (Table S3†). Due to differences in location, the 10 CF_3COO^- ligands are divided into two types (Fig. 3a and S15†): (i) the four with μ_2-η^1:η^1 or μ_3-η^1:η^2 modes cap at the waist; (ii) the six with μ_2-η^1:η^1 mode

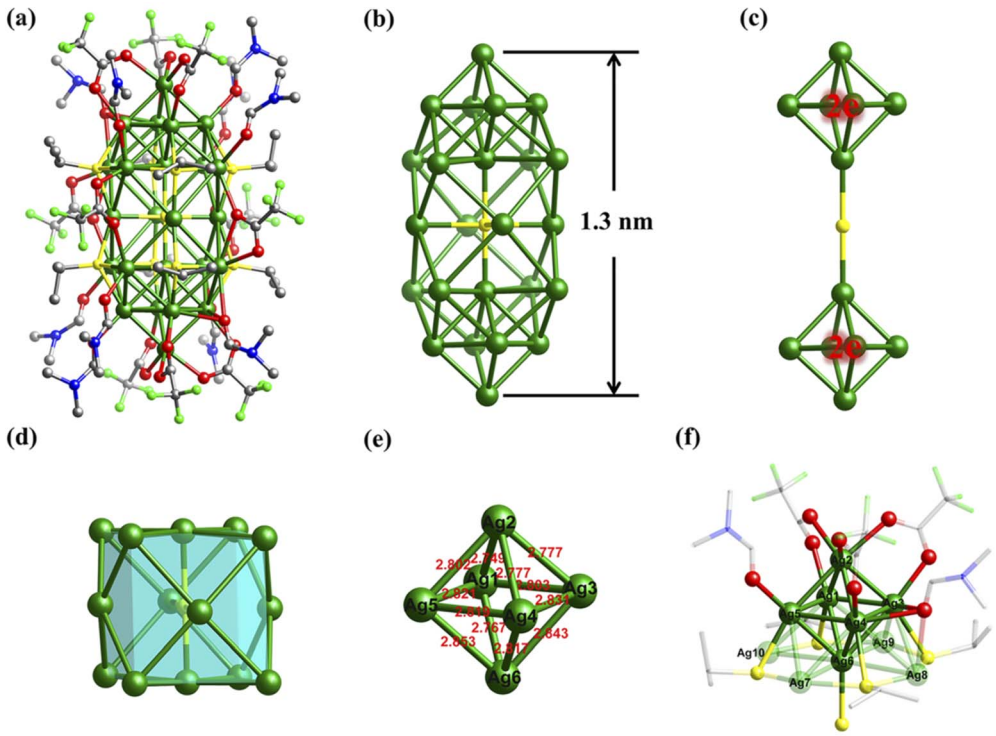

Fig. 3 The crystal structure of Ag_{24}. (a) Ball-and-stick representation of the overall structure. (b) The 'shuttle'-like 24-Ag-atom skeleton. (c) Two Ag_6^{4+} octahedra separated by S^{2-}. (d) The cubic body $S@Ag_{14}$ in the middle of **Ag_{24}**. (e) Structural details and (f) coordination environments of Ag_6^{4+}. Atom color codes: green, Ag; yellow, S; red, O; bright green, F; blue, N; grey, C. All hydrogen atoms are omitted for clarity.

cover the Ag_6. The Ag–O(CF_3COO^-) bond lengths span from 2.26(4) to 2.72(2) Å. Ten additional DMF molecules finally finish the outer organic shell (Ag–O(DMF) bond: 2.27(3) to 2.87(6) Å) to protect and stabilize the S@Ag_{24} kernel (Fig. S16†).

It is worth noting that the Ag···Ag distances of Ag_6 species range from 2.767(4) to 2.853(3) Å with an average of 2.805 Å (Fig. 3e), which is shorter than others (3.057(3) to 3.464(4) Å) of **Ag_{24}** and those of metallic Ag (2.88 Å), indicating the presence of significantly stronger argentophilic interactions. The Ag···Ag distances of the Ag_6 fragments in **Ag_{24}** are comparable to those of reported Ag_6^{4+} cores with similar configurations (2.66–2.87 Å),[10b,16] but shorter than those of Ag_6^{6+} octahedra (2.85–3.44 Å, Table S4†).[10c,17] Therefore, the Ag_6 kernels in **Ag_{24}** should also be Ag_6^{4+} with two delocalized electrons. Moreover, unlike previously reported Ag_6^{4+} octahedra located in the center of the Ag clusters, two Ag_6^{4+} fragments in **Ag_{24}** are on the periphery and stabilized by weak Ag–O bonds (2.27(3) to 2.63(7) Å, Fig. 3f), suggesting that this cluster is highly reactive.

When the **Ag_{24}** crystals were dissolved in CH_2Cl_2, no obvious signal appeared in the ESI-MS spectra. An additional amount of DMF (Fig. S17†) or ^{i}PrOH (Fig. S18†) was introduced, and the ESI-MS spectra showed a series of **Ag_{24}**-related peaks (**1a–1i**, Tables S5; and **2a–2n**, S6†) in both positive and negative ion modes, including the high intensity peak assigned to $[NH_2(CH_3)_2]_4[Ag_{25}S(S^iPr)_8(CF_3COO)_{16}]^-$ (**2d**, calcd m/z = 5322.83) in the mother liquor. These groups of peaks showed strong correlation, which indicated that different numbers of small ions and/or molecules (Ag^+, $NH_2(CH_3)_2^+$, and CF_3COO^-) were attached to the main structure $[Ag_{24}S(S^iPr)_8(CF_3COO)_{10}]$ (Fig. S17f and S18d†). So, **Ag_{24}** is a rare 4e cluster (n = 24–2–8–10) with two independent 2e delocalized Ag_6^{4+} based on the above SCXRD and ESI-MS analysis.

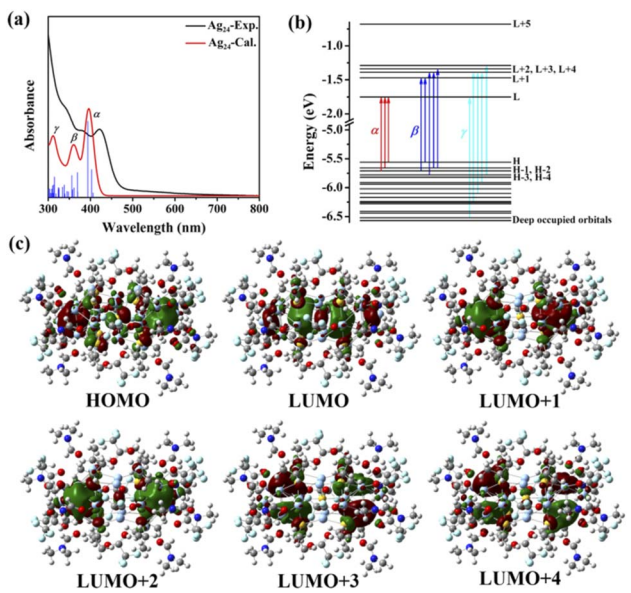

Fig. 4 UV-vis absorption spectra and DFT of Ag_{24}. (a) Experimental (black) and calculated (red) absorption spectra of Ag_{24} in CH_2Cl_2. (b) The Kohn–Sham orbital energy level of Ag_{24}. (c) Frontier orbitals including HOMO, LUMO, LUMO+1, LUMO+2, LUMO+3 and LUMO+4 of Ag_{24}.

The UV-vis spectrum of **Ag_{24}** showed three prominent optical absorption bands at 345, 377 and 422 nm (Fig. 4a). To reveal the electronic structure of **Ag_{24}**, we carried out density functional theory (DFT) and time-dependent density functional theory (TD-DFT) calculations. The calculated spectrum correlated well with the experimental one, and the details of the transitions (α, β, γ; Fig. 4b and S19–S26†) are summarized in Table S7.† The α, β, and γ peaks correspond to HOMO−2/HOMO−1/HOMO → LUMO, HOMO−3/HOMO−2/HOMO−1/HOMO → LUMO+1/LUMO+2/LUMO+3, and HOMO−15/HOMO−10/HOMO−8/HOMO−5/HOMO−3 → LUMO/LUMO+2/LUMO+4 transitions, respectively. The HOMO is composed of two spherical harmonics with S character, originating at the two Ag_6^{4+} centers, while the LUMO, LUMO+1/+2, and LUMO+3/+4 states show 1*P* symmetry at Ag_6^{4+} (Fig. 4c).[10b,16g]

The determination of the key intermediate

Whether **Ag_{24}** is an intermediate in the formation of **Ag_{70}** is the most important issue to reveal the structural evolution and size expansion during the reduction process. To solve this confusion, we tried to obtain the final product (**Ag_{70}**) with **Ag_{24}** crystals as the raw material. When the yellow crystals of **Ag_{24}** were dissolved in MeOH (Video S1†), EtOH or ^{i}PrOH, the color of the solution turned red or brown within 5 s. This means that upon stimulation by solvent molecules, the surface ligands of the highly active **Ag_{24}** were removed, and the more active species clustered to assemble into larger aggregates instead of disintegrating. The ESI-MS spectra of the obtained solution (Fig. 5a and S27†) confirmed the formation of larger species including **Ag_{70}**, which directly confirmed that **Ag_{24}** was a necessary intermediate in the formation of **Ag_{70}**, rather than a simple unrelated kinetic product. The medium-sized {Ag_{49-52}} species observed in the transition process arise as a result of the fragmentation of **Ag_{70}**.[14] Additional CF_3COOAg molecules can inhibit the formation of these fragments (Fig. 5a).

Time-dependent absorption spectra (Fig. 5b) are used to track and monitor the transformation process from **Ag_{24}** (prominent peaks in CH_2Cl_2: 345, 377 and 422 nm) to **Ag_{70}** (distinct absorption bands: 335, 386, 426, 530, and 595 nm in DMF). From 0 h to 6 h, the absorption peaks of 400–450 nm and

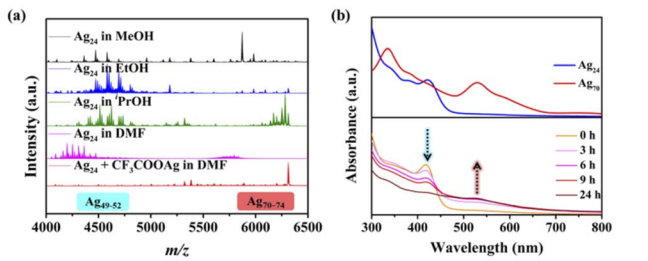

Fig. 5 Tracking the transformation process from Ag_{24} to Ag_{70} by ESI-MS and UV-vis spectroscopy. (a) Negative-ion mode ESI-MS spectra of Ag_{24} in different solutions. (b) Top: UV-vis absorption spectra of Ag_{24} (dissolved in CH_2Cl_2) and Ag_{70} (dissolved in DMF); Bottom: time-dependent UV-vis absorption spectra of Ag_{24} dissolved in DMF for tracking the transformation process from Ag_{24} (yellow solution) to Ag_{70} (red solution).

below 400 nm were attenuated, and the absorption between 450 and 800 nm was enhanced gradually. After 6 h, the spectrum showed three distinct peaks at 340, 423 and 530 nm, and the solution color was changed from yellow to red. Furthermore, ESI-MS was used to analyze the products of the structural conversion (Fig. S28†), and the results were similar to the ESI-MS spectra of **Ag_{24}** dissolved in MeOH. This transition process (**Ag_{24}** → **Ag_{70}**) was slowed down in DMF, possibly due to the presence of a large number of DMF molecules on the cluster surface, which passivated the active Ag_6^{4+} core.

Evolution route from Ag_{24} to Ag_{70}

The growth process of small **Ag_{24}** to **Ag_{70}** by self-reaction is crucial for understanding and controlling the preparation of large-sized Ag nanoclusters. Initial attempts using ESI-MS to identify reaction intermediates in an alcohol solution were unsuccessful because the transition reaction was completed quickly (<1 min). To suppress the reaction kinetics of the system, we tried to trigger reactions of **Ag_{24}** to **Ag_{70}** with mixed solvents (such as CH_2Cl_2 and MeOH, Video S2†). After much trial and error, suitable real-time ESI-MS spectra were obtained for the systems of CH_2Cl_2 + ^{i}PrOH (1 : 1, Fig. 6) and CH_2Cl_2 + DMF (1 : 2, Fig. S29†). As shown in Fig. 6, with the reaction going on, it was clear that the peak intensity of $\{Ag_{24-25}S\}$ (4e) with two negative charges in the m/z = 2250–2750 decreases continuously, while the peaks of **Ag_{70}** began to appear slowly and strengthen. By adjusting the collision voltages and adding CF_3COOAg, it was proved that the group peaks in the m/z = 4100–4900 were the result of the fragmentation of the **Ag_{70}** cluster (Fig. 6a and b). The two systems have similar peak groups and changing trends in negative ion mode ESI-MS (Fig. 6c and S29†). In the positive ion mode ESI-MS, no new peaks appeared in the CH_2Cl_2/^{i}PrOH system, while in CH_2Cl_2/DMF, there were new peaks in the m/z = 4200–4800 denoted as $\{[NH_2(CH_3)_2]_{10+x}Ag_{18+y}S(S^iPr)_5(CF_3COO)_{12+x+y}(DMF)]\}^+$ (x = 0–3, y = 0–1, Fig. S29b–d and Table S8†), containing 8 free valence electrons. The peaks (**4a–4i**) with two negative charges in the m/z = 3500–4000 were assigned to $\{[NH_2(CH_3)_2]_8[Ag_{42+x}S_4(S^iPr)_{11}(CF_3COO)_{9+x}]\}^{2-}$ (x = 0–5, Fig. S30 and Table S9†) containing 24 free valence electrons. The highly reduced $\{Ag_{42-47}S_4\}$ (24e) species with four S^{2-} anions may have formed an initial Ag_nS_4 core similar to the **Ag_{70}** (20e) cluster. Compared to **Ag_{70}** ($[Ag_{70}S_4(S^iPr)_{24}(CF_3COO)_{20}]^{2-}$), the inconsistent electron numbers, and missing metal atoms and ligands of

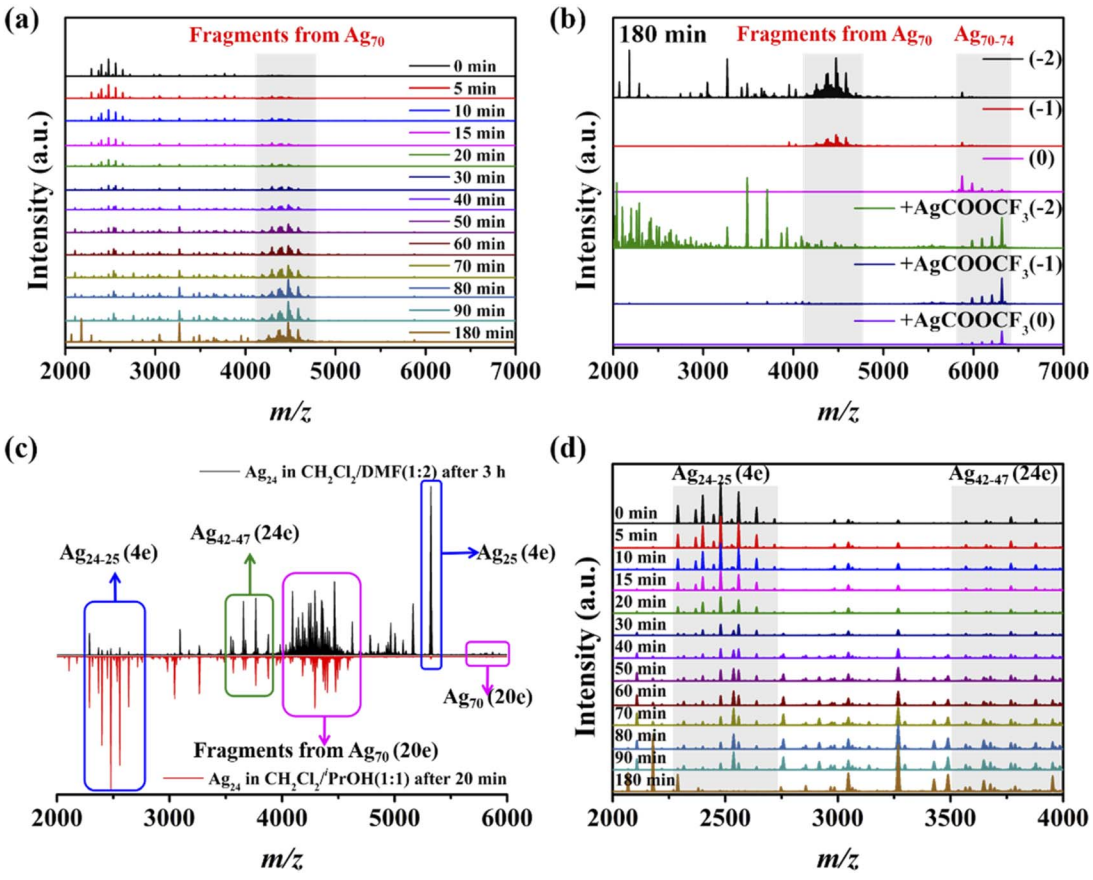

Fig. 6 Time-dependent ESI-MS spectra from **Ag_{24}** to **Ag_{70}** dissolved in the solvent mixture (^{i}PrOH : CH_2Cl_2 = 1 : 1). (a) Time-dependent negative ion mode ESI-MS (collision energy: 2 V) in the range of m/z = 2000–7000 of **Ag_{24}** for tracking the transformation process from **Ag_{24}** to **Ag_{70}**. (b) ESI-MS data at different collision voltages (0, 1, 2 V) after **Ag_{24}** was dissolved in the solvent mixture (^{i}PrOH : CH_2Cl_2 = 1 : 1) for three hours, and ESI-MS data after adding CF_3COOAg salt as a comparison. (c) Comparison of the transformation process from **Ag_{24}** to **Ag_{70}** in different solvents. (d) Time-dependent negative ion mode ESI-MS (collision energy: 2 V) in the range of m/z = 2000–4000, highlighting some key intermediates.

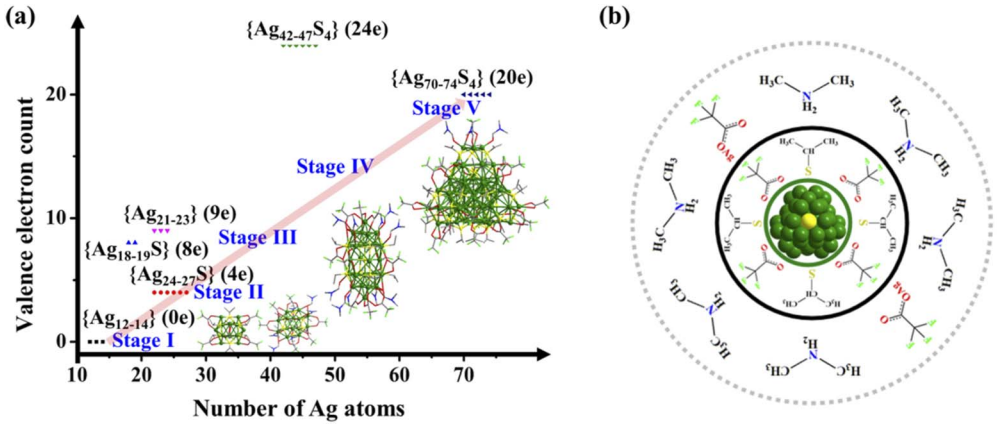

Fig. 7 Schematic illustration of the growth process of Ag_{70} and the general structure of related species. (a) Schematic illustration of the growth process. Five stages dominated by different reaction processes are shown. Stage I: aggregate; stage II: reduction; stage III: decomposition and recombination; stage IV: fusion and stage V: surface recombination and motif enrichment. (b) General structure of relevant clusters during the synthesis of Ag_{70}: Ag–S cores of relevant clusters are protected by organic ligands; $[NH_2(CH_3)_2]^+$ ions and CF_3COOAg molecules are attached to the periphery.

$\{Ag_{42-47}S_4\}$ (24e) suggest that they may still need to undergo oxidation or local decomposition, and further Ag–S shell reconstruction to form the final products. It is worth noting that there are still some peaks that are not assigned properly due to the complexity of the system.

Based on the above observations and analysis, a reasonable stepwise bottom-up evolution route of $\mathbf{Ag_{70}}$ (Fig. 7a) is provided, including five stages: stage I, small molecules (CF_3COOAg and AgS^iPr) aggregate to form stable monovalent clusters, such as $\{Ag_{12-14}\}$; stage II, at a certain acidity, DMF serving as both a mild reducing reagent and an organic reaction medium effectively reduces small Ag fragments (such as $[NH_2(CH_3)_2]_x[Ag_{12+y}(S^iPr)_6(CF_3COO)_{7+x+y}]^-$ (x = 0–4, y = 0–3, $\{Ag_{12-15}\}$ (0e)), Fig. S7–S9†) to classical face-centered cubic (fcc) Ag_6^{4+} species. The Ag_6^{4+} reducing fragments are passivated by S^{2-} templates *in situ* generated from the breaking of the S–C bond of organic ligands, forming relatively stable $\{Ag_{24-27}S\}$ (4e) clusters containing a $S@(Ag_6)_2$ skeleton (Fig. 2 and S17, S18†); stage III, $\mathbf{Ag_{24}}$ disintegrate and recombine to form intermediates with more free electrons, such as $\{[NH_2(CH_3)_2]_3[Ag_{21+x}(S^iPr)_5(CF_3COO)_{11+x}]\}^-$ (x = 0–2, $\{Ag_{21-23}\}$ (9e), Fig. 2 and S7–S9†) and $\{[NH_2(CH_3)_2]_{10+x}Ag_{18+y}S(S^iPr)_5(CF_3COO)_{12+x+y}(DMF)]\}^+$ (x = 0–3, y = 0–1, $\{Ag_{18-19}S\}$ (8e), Fig. S29†); stage IV, the small reducing products described above assemble and fuse together to form 4 S^{2-}-passivated preliminary products, $\{[NH_2(CH_3)_2]_8[Ag_{42+x}S_4(S^iPr)_{11}(CF_3COO)_{9+x}]\}^{2-}$ (x = 0–5, $\{Ag_{42-47}S_4\}$ (24e), Fig. S30 and Table S9†); stage V, on the basis of $\{Ag_{42-47}S_4\}$ (24e), oxidation or localized decomposition occurs and extra small molecules accumulate on the surface to form the final product $\mathbf{Ag_{70}}$ (Fig. S31†) with a multi-S^{2-}-passivated Ag_{28}^{8+} kernel (20e) possessing an fcc Ag_{16} inner core. It can be seen that the formation process of $\mathbf{Ag_{70}}$ nanoclusters is different from that of typical Ag NCs (lowly reduced species with a similar number of metal as the product is formed first, and is further reduced) and Au NCs (step-by-step formation process).[11]

Interestingly, these observed intermediate species and products have similar structural features (Fig. 7b): the silver or silver–sulfur framework protected by organic ligands (CF_3COO^- and S^iPr^-) is always enriched with some $[NH_2(CH_3)_2]^+$ ions and CF_3COOAg molecules based on electrostatic and hydrogen bonding interactions at the periphery. The introduction of additional $[NH_2(CH_3)_2]^+$ cations can significantly improve yields, as do other similar amine cations. These species are critical for stabilizing intermediates and forming products. Uncovering the formation process of this medium-scale nanocluster is of great importance since it maps out a reasonable and common avenue for the generation and expansion of the fcc metal kernel in metal nanoclusters.

Conclusions

In summary, the reaction process of $\mathbf{Ag_{70}}$ was traced by time-dependent UV-vis spectroscopy and ESI-MS. The intermediates ($\mathbf{Ag_{14}}$ and $\mathbf{Ag_{24}}$) were crystallized successfully by controlling the reaction time. A reasonable path from Ag^+ species (such as $\mathbf{Ag_{14}}$) to $\mathbf{Ag_{24}}$ (skeleton: $S@(Ag_6^{4+})_2$), and then to $\mathbf{Ag_{70}}$ (multi-S^{2-} induced kernel: Ag_{28}^{8+}) has been mapped out. The detailed process of bottom-up assembly from $\mathbf{Ag_{24}}$ to $\mathbf{Ag_{70}}$ was successfully revealed by real-time ESI-MS. The evolutionary route suggests that small cations for stabilization and highly reactive reducing species are critical for the formation of large-sized Ag NCs. Overall, this work presents a reasonable avenue for comprehending the generation and expansion of an fcc core in metal NCs, and provides some guidance for controlled synthesis of NCs and nanoparticles in the future.

Data availability

All the data supporting this article have been included in the main text and the ESI.† The X-ray crystallographic coordinates for structures reported inthis article have been deposited at the

Cambridge Crystallographic Data Centre (CCDC) under deposition numbers CCDC: 2182448, 2182449, and 2182450.

Author contributions

S. Q. Z. conceived and designed the experiments. X. M. L. and S. H. conducted the synthesis and characterization. X. M. L. drew the pictures in the manuscript. S. Q. Z., X. Y. D. and X. M. L. analysed the experimental results. X. M. L. and K. M. completed crystallographic data collection and refinement of the structure. P. L. performed the calculations. Z. Y. W. helped to revise the writing. X. M. L., X. Y. D., and S. Q. Z. co-wrote the manuscript.

Conflicts of interest

There are no conflicts to declare.

Acknowledgements

This work was supported by the National Natural Science Foundation of China (No. 21825106, U21A20277, 92061201, and 21975065) and Zhengzhou University.

References

1 (*a*) Y. Li, M. Zhou, Y. Song, T. Higaki, H. Wang and R. Jin, *Nature*, 2021, **594**, 380–384; (*b*) Q. Yao, T. Chen, X. Yuan and J. Xie, *Acc. Chem. Res.*, 2018, **51**, 1338–1348.

2 (*a*) Y. Jin, C. Zhang, X.-Y. Dong, S.-Q. Zang and T. C. W. Mak, *Chem. Soc. Rev.*, 2021, **50**, 2297–2319; (*b*) Y.-P. Xie, J.-L. Jin, G.-X. Duan, X. Lu and T. C. W. Mak, *Coord. Chem. Rev.*, 2017, **331**, 54–72.

3 (*a*) O. Fuhr, S. Dehnen and D. Fenske, *Chem. Soc. Rev.*, 2013, **42**, 1871–1906; (*b*) M.-M. Zhang, X.-Y. Dong, Y.-J. Wang, S.-Q. Zang and T. C. W. Mak, *Coord. Chem. Rev.*, 2022, **453**, 214315.

4 I. Chakraborty and T. Pradeep, *Chem. Rev.*, 2017, **117**, 8208–8271.

5 Y. Li, T. Higaki, X. Du and R. Jin, *Adv. Mater.*, 2020, **32**, 1905488.

6 X. Kang and M. Zhu, *Chem. Soc. Rev.*, 2019, **48**, 2422–2457.

7 (*a*) J. Yan, B. K. Teo and N. Zheng, *Acc. Chem. Res.*, 2018, **51**, 3084–3093; (*b*) R. Jin, G. Li, S. Sharma, Y. Li and X. Du, *Chem. Rev.*, 2021, **121**, 567–648.

8 R. W. Huang, Y. S. Wei, X. Y. Dong, X. H. Wu, C. X. Du, S. Q. Zang and T. C. W. Mak, *Nat. Chem.*, 2017, **9**, 689–697.

9 (*a*) X. Zhao, S.-Q. Zang and X. Chen, *Chem. Soc. Rev.*, 2020, **49**, 2481–2503; (*b*) R. R. Nasaruddin, T. Chen, Q. Yao, S. Zang and J. Xie, *Coord. Chem. Rev.*, 2021, **426**, 213540.

10 (*a*) Q. Li, B. Huang, S. Yang, H. Zhang, J. Chai, Y. Pei and M. Zhu, *J. Am. Chem. Soc.*, 2021, **143**, 15224–15232; (*b*) X.-M. Luo, C.-H. Gong, X.-Y. Dong, L. Zhang and S.-Q. Zang, *Nano Res.*, 2021, **14**, 2309–2313; (*c*) M.-Y. Gao, K. Wang, Y. Sun, D. Li, B.-Q. Song, Y. H. Andaloussi, M. J. Zaworotko, J. Zhang and L. Zhang, *J. Am. Chem. Soc.*, 2020, **142**, 12784–12790; (*d*) Y.-J. Zhong, J.-H. Liao, T.-H. Chiu, S. Kahlal, C.-J. Lin, J.-Y. Saillard and C. W. Liu, *Angew. Chem., Int. Ed.*, 2021, **60**, 12712–12716.

11 (*a*) Y. Cao, T. Chen, Q. Yao and J. Xie, *Acc. Chem. Res.*, 2021, **54**, 4142–4153; (*b*) Y. Cao, T. Liu, T. Chen, B. Zhang, D.-e. Jiang and J. Xie, *Nat. Commun.*, 2021, **12**, 3212; (*c*) Y. Cao, V. Fung, Q. Yao, T. Chen, S. Zang, D.-e. Jiang and J. Xie, *Nat. Commun.*, 2020, **11**, 5498; (*d*) Q. Yao, X. Yuan, V. Fung, Y. Yu, D. T. Leong, D.-e. Jiang and J. Xie, *Nat. Commun.*, 2017, **8**, 927; (*e*) Z. Luo, V. Nachammai, B. Zhang, N. Yan, D. T. Leong, D.-e. Jiang and J. Xie, *J. Am. Chem. Soc.*, 2014, **136**, 10577–10580; (*f*) T. Chen, V. Fung, Q. Yao, Z. Luo, D.-e. Jiang and J. Xie, *J. Am. Chem. Soc.*, 2018, **140**, 11370–11377; (*g*) Y. Cao, J. Guo, R. Shi, G. I. N. Waterhouse, J. Pan, Z. Du, Q. Yao, L.-Z. Wu, C.-H. Tung, J. Xie and T. Zhang, *Nat. Commun.*, 2018, **9**, 2379.

12 Z. Lei, J.-J. Li, Z.-A. Nan, Z.-G. Jiang and Q.-M. Wang, *Angew. Chem., Int. Ed.*, 2021, **60**, 14415–14419.

13 (*a*) J.-H. Huang, Y. Si, X.-Y. Dong, Z.-Y. Wang, L.-Y. Liu, S.-Q. Zang and T. C. W. Mak, *J. Am. Chem. Soc.*, 2021, **143**, 12439–12444; (*b*) X. Liu, G. Saranya, X. Huang, X. Cheng, R. Wang, M. Chen, C. Zhang, T. Li and Y. Zhu, *Angew. Chem., Int. Ed.*, 2020, **59**, 13941–13946; (*c*) F. Hu, J.-J. Li, Z.-J. Guan, S.-F. Yuan and Q.-M. Wang, *Angew. Chem., Int. Ed.*, 2020, **59**, 5312–5315; (*d*) F. Hu, Z.-J. Guan, G. Yang, J.-Q. Wang, J.-J. Li, S.-F. Yuan, G.-J. Liang and Q.-M. Wang, *J. Am. Chem. Soc.*, 2021, **143**, 17059–17067.

14 X.-M. Luo, C.-H. Gong, F. Pan, Y. Si, J.-W. Yuan, M. Asad, X.-Y. Dong, S.-Q. Zang and T. C. W. Mak, *Nat. Commun.*, 2022, **13**, 1177.

15 M.-H. Du, L.-Q. Chen, L.-P. Jiang, W.-D. Liu, L.-S. Long, L. Zheng and X.-J. Kong, *J. Am. Chem. Soc.*, 2022, **144**, 5653–5660.

16 (*a*) X.-Q. Liang, Y.-Z. Li, Z. Wang, S.-S. Zhang, Y.-C. Liu, Z.-Z. Cao, L. Feng, Z.-Y. Gao, Q.-W. Xue, C.-H. Tung and D. Sun, *Nat. Commun.*, 2021, **12**, 4966; (*b*) G. Deng, S. Malola, P. Yuan, X. Liu, B. K. Teo, H. Häkkinen and N. Zheng, *Angew. Chem., Int. Ed.*, 2021, **60**, 12897–12903; (*c*) A. K. Das, R. Mekkat, S. Maity, A. S. Nair, S. Bhandary, R. Bhowal, A. Patra, B. Pathak, D. Chopra and S. Mandal, *Inorg. Chem.*, 2021, **60**, 19270–19277; (*d*) Z. Wang, Q.-P. Qu, H.-F. Su, P. Huang, R. K. Gupta, Q.-Y. Liu, C.-H. Tung, D. Sun and L.-S. Zheng, *Sci. China: Chem.*, 2020, **63**, 16–20; (*e*) Q. Sun, H.-H. Nie, H.-F. Su, S.-Y. Yang and B. K. Teo, *Inorg. Chem.*, 2020, **59**, 8836–8845; (*f*) Z. Wang, F.-L. Yang, Y. Yang, Q.-Y. Liu and D. Sun, *Chem. Commun.*, 2019, **55**, 10296–10299; (*g*) Z.-Y. Wang, M.-Q. Wang, Y.-L. Li, P. Luo, T.-T. Jia, R.-W. Huang, S.-Q. Zang and T. C. W. Mak, *J. Am. Chem. Soc.*, 2018, **140**, 1069–1076; (*h*) Z. Wang, H.-F. Su, M. Kurmoo, C.-H. Tung, D. Sun and L.-S. Zheng, *Nat. Commun.*, 2018, **9**, 2094; (*i*) S. Chen, W.-H. Fang, L. Zhang and J. Zhang, *Angew. Chem., Int. Ed.*, 2018, **57**, 11252–11256; (*j*) H. Yang, J. Lei, B. Wu, Y. Wang, M. Zhou, A. Xia, L. Zheng and N. Zheng, *Chem. Commun.*, 2013, **49**, 300–302; (*k*) Y. Kikukawa, Y. Kuroda, K. Suzuki, M. Hibino, K. Yamaguchi and N. Mizuno, *Chem. Commun.*, 2013, **49**, 376–378; (*l*) K. Yonesato, H. Ito, H. Itakura, D. Yokogawa, T. Kikuchi, N. Mizuno, K. Yamaguchi and K. Suzuki, *J. Am. Chem. Soc.*, 2019, **141**, 19550–19554; (*m*) G. Deng, B. K. Teo and N. Zheng, *J. Am. Chem. Soc.*, 2021, **143**, 10214–10220;

(*n*) G. Deng, S. Malola, P. Yuan, X. Liu, B. K. Teo, H. Hakkinen and N. Zheng, *Angew. Chem., Int. Ed.*, 2021, **60**, 12897–12903; (*o*) S. Chen, W. H. Fang, L. Zhang and J. Zhang, *Angew. Chem., Int. Ed.*, 2018, **57**, 11252–11256.

17 (*a*) Z. Wang, J.-W. Liu, H.-F. Su, Q.-Q. Zhao, M. Kurmoo, X.-P. Wang, C.-H. Tung, D. Sun and L.-S. Zheng, *J. Am. Chem. Soc.*, 2019, **141**, 17884–17890; (*b*) Z. Han, X.-Y. Dong, P. Luo, S. Li, Z.-Y. Wang, S.-Q. Zang and C. W. Mak Thomas, *Sci. Adv.*, 2020, **6**, eaay0107.